energies

MDPI

Article

Design and Analysis of a Low Torque Ripple Permanent Magnet Synchronous Machine for Flywheel Energy Storage Systems

Yubo Sun [1,*], Zhenghui Zhao [2] and Qian Zhang [3]

[1] Department of Electrical Engineering, Tsinghua University, Beijing 100084, China
[2] School of Electrical Information Engineering, Jiangsu University, Zhenjiang 212013, China; zhzhao@ujs.edu.cn
[3] School of Agricultural Engineering, Jiangsu University, Zhenjiang 212013, China; zhangq_jsu@ujs.edu.cn
* Correspondence: sunyb16@mails.tsinghua.edu.cn

Abstract: Flywheel energy storage systems (FESS) are technologies that use a rotating flywheel to store and release energy. Permanent magnet synchronous machines (PMSMs) are commonly used in FESS due to their high torque and power densities. One of the critical requirements for PMSMs in FESS is low torque ripple. Therefore, a PMSM with eccentric permanent magnets is proposed and analyzed in this article to reduce torque ripple. Cogging torque, a significant contributor to torque ripple, is investigated by a combination of finite element analysis and the analytical method. An integer-slot distribution winding structure is adopted to reduce vibration and noise. Moreover, the effects of eccentric permanent magnets and harmonic injection on the cogging torque are analyzed and compared. In addition, the electromagnetic performance is analyzed, and the torque ripple is found to be 3.1%. Finally, a prototype is built and tested, yielding a torque ripple of 3.9%, to verify the theoretical analysis.

Keywords: eccentric permanent magnet; flywheel energy storage system; harmonic injection; low torque ripple; permanent magnet synchronous machine

Citation: Sun, Y.; Zhao, Z.; Zhang, Q. Design and Analysis of a Low Torque Ripple Permanent Magnet Synchronous Machine for Flywheel Energy Storage Systems. *Energies* **2024**, *17*, 6337. https://doi.org/10.3390/en17246337

Academic Editor: Kwok Tong Chau

Received: 20 November 2024
Revised: 11 December 2024
Accepted: 13 December 2024
Published: 16 December 2024

1. Introduction

In recent years, flywheel energy storage systems (FESS) have gained significant attention due to their large-capacity energy storage capabilities in the field of renewable energy [1]. FESS are technologies that use a rotating flywheel to store and release energy. FESS convert electrical energy into mechanical energy for storage and then revert it to electrical energy when needed [2,3]. However, FESS are only used for the short-term storage of electrical energy [4]. Consequently, FESS are very suitable for stabilizing grid load fluctuations and providing backup power [5]. FESS can deliver power for short durations to maintain stable operation during main power supply failures. As the core component of FESS, the machine must exhibit high torque density [6], high efficiency [7], and high reliability [8]. Therefore, various machines are utilized in FESS to fulfill actual requirements [9,10].

With the ongoing advancement of magnetic material technology, rare-earth permanent magnet synchronous machines (PMSMs) have demonstrated strong application potential across various fields, owing to their simple structure [11], reliable operation [12], low loss [13], and high efficiency [14]. Moreover, due to their high torque and power densities, PMSMs are highly suitable as the electric machines in FESS. Although PMSMs are widely used in FESS, these systems require machines to provide high average torque and low torque ripple to avoid large vibration and noise. In practical applications, PMSMs exhibit torque ripple due to their inherent characteristics. The level of torque ripple is a critical performance indicator for the electric machines in FESS. PMSMs with low torque ripple can enhance system smoothness, reduce mechanical wear, increase efficiency, improve control accuracy and decrease electromagnetic interference. Low torque ripple is crucial

in applications requiring high electromagnetic performance. Therefore, it is necessary to conduct research on reducing the torque ripple of PMSMs.

In recent years, numerous studies have focused on reducing the torque ripple. Cogging torque is an important cause of torque ripple. The reduction in cogging torque can be approached from two perspectives, including optimizing the topology and refining the control strategy [15,16]. In Wang et al. [17], a method to suppress the torque ripple of the traditional V-shaped permanent magnet vernier machine was proposed. The generation mechanism of cogging torque as the major source of the torque ripple is explained based on the magnetic field modulation principle. The results indicate that the torque ripple is suppressed effectively based on the shifted permeance method. In Du et al. [18], various design techniques for torque ripple reduction were compared. The new axial pole shaping technique achieves a specific flux concentration pattern on the rotor surface along the axial direction through shaping the pole arc radially and axially. The comparative study shows that the axial pole shaping can reduce the torque ripple effectively with minimum torque reduction compared to the other traditional techniques. In Wu et al. [19], an improved scheme for torque ripple reduction in PMSMs was proposed. Different from the previous methods, both q-axis and d-axis harmonic currents were optimized and injected. In Shimizu et al. [20], guidelines for reducing the torque ripple of multilayer interior PMSM were determined. The torque ripple of a double-layer interior PMSM with holes drilled in the rotor core was suppressed by 54.8% compared with the reference model. However, the torque ripple of the PMSM remains high at 11.6%. In Xu et al. [21], an auxiliary notch design method for the interior PMSM for suppressing torque ripple was proposed. After using auxiliary notch design, the torque ripple was significantly reduced and the torque amplitude was almost not sacrificed. However, the existing literature rarely considers the combination of finite element analysis and the analytical method to investigate the torque ripple.

The purpose of this article is to propose a low torque ripple PMSM for FESS. One of the critical requirements for PMSMs in FESS is low torque ripple. A combination of finite element analysis and the analytical method is employed to investigate the cogging torque of the PMSM. The effects of eccentric permanent magnets and harmonic injection on the cogging torque are, respectively, analyzed. By calculating the contribution of various harmonics to the cogging torque, the underlying causes of torque ripple reduction are clarified. Considering the torque performance, the eccentric design of the permanent magnets is adopted to the PMSM. The rest of this article is organized as follows. In Section 2, the topology and structure parameters of the low torque ripple PMSM are described. In Section 3, the analytical method is employed to analyze the cogging torque. Additionally, the effects of eccentric permanent magnets and harmonic injection on the cogging torque are compared. In Section 4, the electromagnetic performance is analyzed. In Section 5, the theoretical analysis is verified through experiments. Finally, this article is concluded in Section 6.

2. Machine Topology

The selection of slot-pole count significantly influences the electromagnetic performance of the PMSM. When the stator outer diameter is fixed, a small number of slots requires more conductors per slot to meet the torque requirements. The cross-sectional area of the winding increases, making it difficult to bend during winding. On the other hand, a large number of slots results in narrower stator teeth, which can reduce the mechanical strength of the core and lower the slot utilization. Thus, selecting the optimal slot-pole count presents a challenge in balancing both power density and torque ripple. By increasing the least common multiple of the number of slots and poles, both the winding coefficient and the suppression of torque ripple can be improved. Additionally, in order to avoid low-order radial electromagnetic force harmonics, the greatest common divisor of the number of slots and poles should be increased. Consequently, a 36-slot, 12-pole integer-slot distributed winding scheme is adopted for the PMSM in FESS, resulting in a winding coefficient of 1. The design requirements for the PMSM are listed in Table 1.

Table 1. Requirements for PMSM.

Item	Requirement
Operating voltage	175~320 V
Rated power	3 kW
Rotating speed	2500 rpm
Cooling method	Natural cooling

Figure 1 presents the topology of the low torque ripple PMSM for FESS. It can be seen that the proposed PMSM consists of two parts, including the outer stator and inner rotor. As the rated speed of the PMSM is 2500 rpm, a surface-mounted rotor structure is adopted after consideration. The permanent magnets are attached to the surface of the rotor. A high-temperature-resistant material is chosen for the permanent magnets to prevent irreversible demagnetization and ensure long-term, stable operation in high-temperature environments. In addition, by optimizing the polar arc shape of the permanent magnets, the magnetic flux density distribution in the air gap is close to a sinusoidal shape, which can reduce the cogging torque and torque ripple. Consequently, an eccentric design of the permanent magnets is adopted in the PMSM to reduce the torque ripple. The winding connection diagram of the PMSM for FESS is shown in Figure 2. It is evident that the serial numbers correspond to the slot numbers. The winding is divided into three phases, with each phase consisting of six coils connected in series. These six coils are sequentially connected, and each group of coils is wound in three strands, with 36 turns per strand. The armature winding of the PMSM for FESS features a single-layer structure, ensuring strong phase independence. Additionally, the integer-slot distribution winding structure has little impact on vibration and noise. Moreover, the structure parameters of the PMSM for FESS are listed in Table 2.

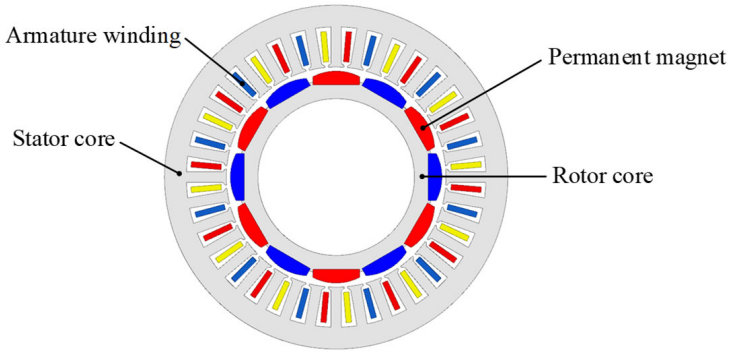

Figure 1. Topology of proposed PMSM.

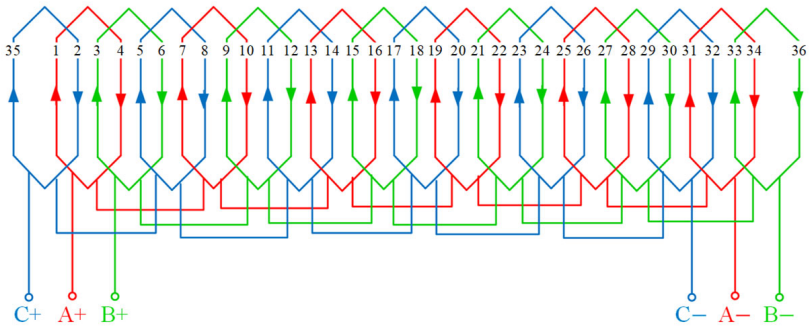

Figure 2. Winding connection.

Table 2. Structure parameters of PMSM.

Item	Value
Stator slot number	36
Rotor polo number	12
Winding coefficient	1
Stator outer diameter/mm	125
Stator inner diameter/mm	80
Air gap length/mm	1.5
Axial length/mm	90
Permanent magnet thickness/mm	5
Number of turns	36
Stator core	B35AH230
Rotor core	B35AH230
Permanent magnet	Sm32

3. Torque Ripple Suppression and Performance Analysis

3.1. Cogging Torque Analysis

The selection of integer-slot distribution winding structure exacerbates the issue of cogging torque, leading to torque ripple. Therefore, effectively suppressing cogging torque is crucial. The calculation methods for analyzing cogging torque typically include the finite element method and the analytical method. In order to further investigate the principle of cogging torque reduction, the analytical method is employed to analyze the cogging torque of the surface-mounted PMSM. The analysis model of the surface-mounted PMSM is depicted in Figure 3. It can be seen that R_r and R_m represent the inner and outer radii of the permanent magnet, respectively. R_s and R_{sb} denote the inner radius of the stator core and the radius at the bottom of the stator slot, respectively.

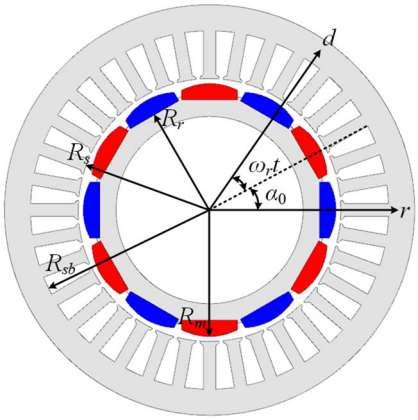

Figure 3. Analysis model of surface-mounted PMSM.

Assuming that the core permeability is infinite, the permanent magnet and air gap are taken as the solution area. In the solution area, the magnetic induction intensity and magnetic field strength satisfy the following requirements, respectively:

$$\begin{cases} B = \mu_0 H & \text{(In air gap)} \\ B = \mu_0 \mu_r H + \mu_0 M & \text{(In permanent magnet)} \end{cases} \quad (1)$$

where μ_0 is the vacuum permeability, μ_r is the relative permeability of the permanent magnet, M is the residual magnetization in the permanent magnet, B is the magnetic flux density, and H is the magnetic field strength.

The no-load magnetic field of the PMSM is calculated by using the scalar potential equation. In the polar coordinate system, the scalar potential φ satisfies the Laplace equation as follows:

$$\begin{cases} \frac{\partial^2 \varphi_1}{\partial r^2} + \frac{1}{r}\frac{\partial \varphi_1}{\partial r} + \frac{1}{r^2}\frac{\partial^2 \varphi_1}{\partial \alpha^2} = \frac{M_r}{r\mu_r} & \text{(In permanent magnet)} \\ \frac{\partial^2 \varphi_2}{\partial r^2} + \frac{1}{r}\frac{\partial \varphi_2}{\partial r} + \frac{1}{r^2}\frac{\partial^2 \varphi_2}{\partial \alpha^2} = 0 & \text{(In air gap)} \end{cases} \tag{2}$$

where r and α are the pole diameter and polar angle in the polar coordinate system and M_r is the radial component of the residual magnetization of the permanent magnet. In order to solve the scalar potential, the following boundary conditions are established.

1. The boundary condition of the surface-mounted PMSM at the intersection of the rotor core and the surface of the permanent magnet can be expressed as

$$H_{\alpha 1}(r,\alpha)|_{r=R_r} = 0 \tag{3}$$

2. The boundary condition at the surface of the permanent magnet near the side of the air gap can be expressed as

$$\begin{aligned} H_{\alpha 1}(r,\alpha)|_{r=R_m} &= H_{\alpha 2}(r,\alpha)|_{r=R_m} \\ B_{r1}(r,\alpha)|_{r=R_m} &= B_{r2}(r,\alpha)|_{r=R_m} \end{aligned} \tag{4}$$

3. The boundary condition at the surface of the stator core near the side of the air gap can be expressed as

$$B_{r2}(r,\alpha)|_{r=R_s} = B_s(\alpha) \tag{5}$$

where the subscripts 1 and 2 represent the regions where each variable is located, and the subscripts r and α represent the radial and tangential components corresponding to the magnetic induction intensity B and the magnetic field strength H.

According to the relationship between magnetic induction intensity, magnetic field strength, scalar magnetic potential, and the boundary conditions of the magnetic field, the radial air gap magnetic density and tangential air gap magnetic density can be expressed as [22]

$$\begin{aligned} B_{rg} &= \sum_k B_{rck}\cos k\alpha + \sum_k B_{rsk}\sin k\alpha \\ B_{\alpha g} &= \sum_k B_{\alpha ck}\cos k\alpha + \sum_k B_{\alpha sk}\sin k\alpha \end{aligned} \tag{6}$$

where B_{rck}, B_{rsk}, $B_{\alpha ck}$ and $B_{\alpha sk}$ are the harmonic amplitudes of the kth radial air gap magnetic density and tangential air gap magnetic density, respectively. In addition, B_{rck} can be expressed as

$$B_{rck} = A_{4k}\cos(k\omega_r t + k\alpha_0)[\gamma(k)M_{rk} + \zeta(k)M_{\alpha k}]f_{Br} - g_{Br}\sum_i\sum_m C_{ei}(m)\eta_{si}(m,k) \tag{7}$$

where ω_r is the rotor speed, α_0 is the initial position of the rotor, k, i and m are the harmonic orders, and the coefficients A_{4k}, γ, ζ, f_{Br}, g_{Br}, C_{ei}, η, M_{rk}, and $M_{\alpha k}$ are consistent with those in [22].

Based on Maxwell stress tensor method, the cogging torque can be obtained from the air gap magnetic density and expressed as [23]

$$T_{cogg} = \frac{l_a r^2}{\mu_0}\int_0^{2\pi} B_r B_\alpha d\alpha = \frac{\pi l_a r^2}{\mu_0}\sum_k (B_{rck}B_{\alpha ck} + B_{rsk}B_{\alpha sk}) = \sum_k T_{ck} \tag{8}$$

where l_a is the effective length of the PMSM, and T_{ck} is the cogging torque component generated by the kth air gap magnetic density harmonics. Therefore, T_{ck} can be expressed as

$$T_{ck} = \frac{\pi l_a r^2}{\mu_0} B_{rk}B_{\alpha k}\cos(\alpha_{rk} - \alpha_{\alpha k}) \tag{9}$$

3.2. Effect of Eccentric Permanent Magnet on Cogging Torque

In contrast to shingle-type permanent magnets, bread-type permanent magnets feature a flat bottom and exhibit an uneven thickness distribution. The eccentric design of the bread-type permanent magnets has a huge influence on the cogging torque of the PMSM. The bread-type eccentric permanent magnet is shown in Figure 4. It is evident that O is the center of the original permanent magnet. When the permanent magnet is eccentric, the outer radius O_1 moves upward, resulting in a distance h between O and O_1, which represents the eccentricity. According to the geometric relationship in Figure 3, the outside radius OA_1 of the eccentric permanent magnet can be expressed as

$$OA_1 = R_m(\theta) = h\cos\theta + \sqrt{R_1^2 - (h\sin\theta)^2} = h\cos\theta + \sqrt{(R_s - g - h)^2 - (h\sin\theta)^2} \quad (10)$$

where g is the length of the air gap, h is the eccentricity, p is the number of pole-pairs, α_p is the polar arc coefficient, and θ is the angle between the outer radius OA_1 and the center of the permanent magnet. The range of θ is $[-\pi\alpha_p/2p, \pi\alpha_p/2p]$. As a result, the outer radius of the eccentric permanent magnet can be calculated, and it varies with the eccentricity.

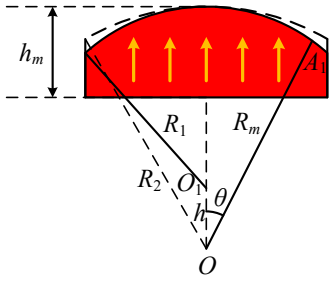

Figure 4. Bread-type eccentric permanent magnet.

The eccentricity of the permanent magnet significantly affects the torque performance of the PMSM. Figure 5 shows the variation in the torque performance with respect to the eccentricity h. It can be observed that both the peak cogging torque and torque ripple decrease as eccentricity increases. When the eccentricity is less than 20 mm, there is a significant reduction in both the peak cogging torque and torque ripple. However, when the eccentricity exceeds 20 mm, the rate of decrease becomes less pronounced. Since the eccentric design of the permanent magnet reduces the amount of magnet material, the torque is also reduced. Moreover, the eccentric design causes the air gap to be unevenly distributed, affecting the waveform of the air gap magnetic density. Considering the torque performance of the PMSM, the eccentricity h is selected to be 20 mm.

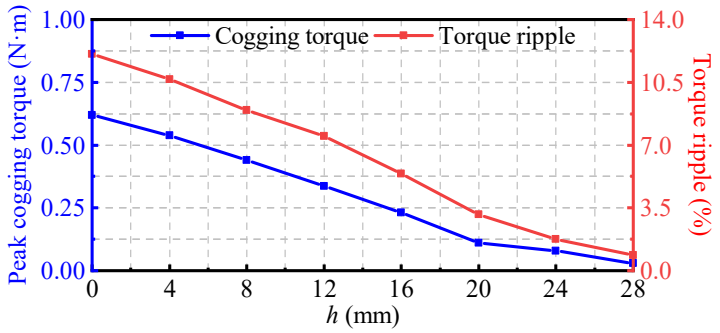

Figure 5. Influence of eccentricity on torque performance.

The cogging torque of the PMSM is analyzed using finite element analysis, both with and without eccentric permanent magnets, as illustrated in Figure 6. The results demonstrate that the eccentric design significantly weakens the cogging torque, reducing

it from 0.62 N·m to 0.11 N·m. In order to further investigate the causes of the cogging torque reduction, a combination of finite element analysis and the analytical method is employed to assess the contribution of various harmonics to the cogging torque. The radial and tangential air gap magnetic densities of the PMSM, both with and without eccentric permanent magnets, are compared and analyzed, as shown in Figure 7a,b. It is evident that the eccentric permanent magnets cause the air gap to become uneven, and the air gap magnetic density waveforms more closely approximate a sinusoidal shape. Fourier decomposition is performed on the air gap magnetic densities, as shown in Figure 7c. It is apparent that the air gap magnetic densities are primarily composed of the 6th, 18th, and 30th harmonics, with the 6th harmonic being the most dominant. The eccentric design does not introduce new harmonic orders, but it reduces the amplitude of the radial and tangential air gap magnetic density harmonics, with the most significant reduction observed in the 18th harmonic.

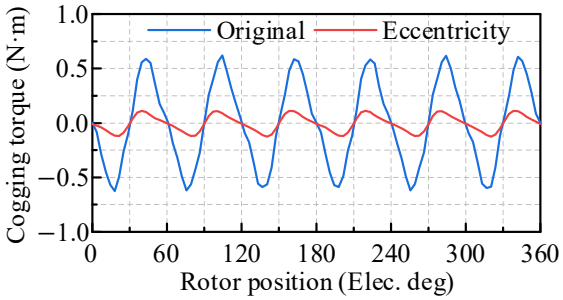

Figure 6. Cogging torque of PMSM with different permanent magnets.

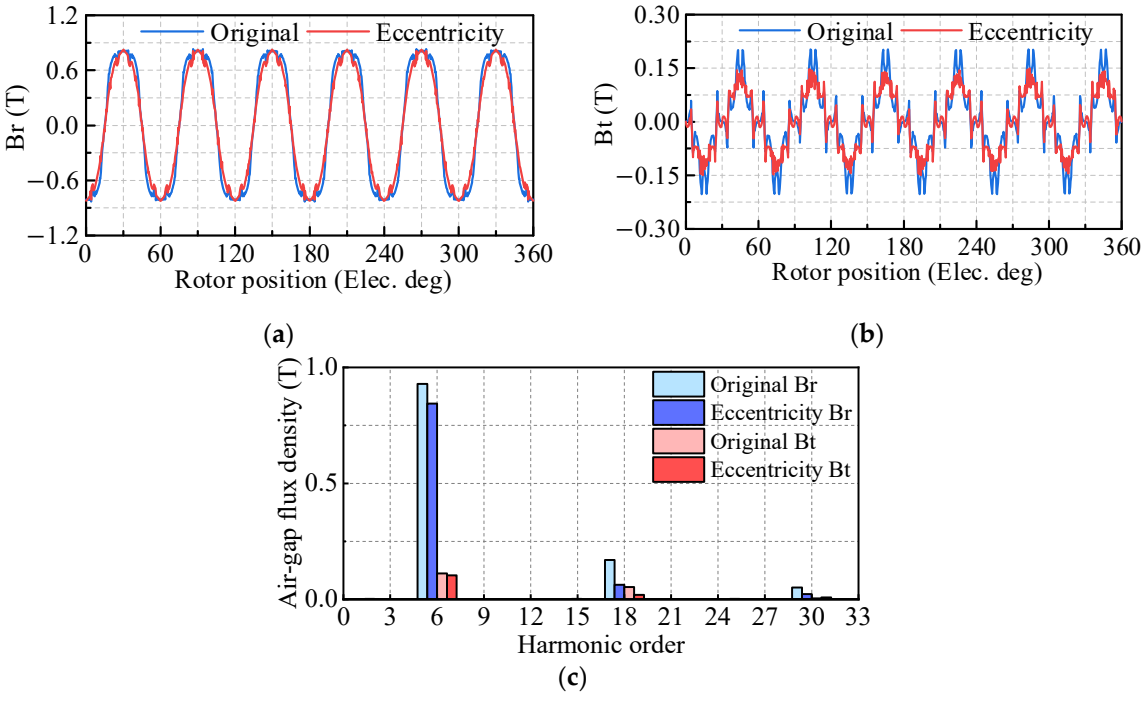

Figure 7. Air gap magnetic densities of PMSM with different permanent magnets. (**a**) Radial air gap magnetic densities. (**b**) Tangential air gap magnetic densities. (**c**) Harmonic order.

The contribution of each harmonic order to the cogging torque is shown in Figure 8. The cogging torque generated by the *k*th harmonic can be calculated. The total cogging torque of the PMSM with the original permanent magnets is primarily composed of the cogging torque generated by the 6th, 18th, 30th, and 42nd harmonics. The superimposed cogging torque waveform closely matches the waveform obtained from finite element

simulations. The 30th harmonic is the largest contributor to the total cogging torque of the PMSM with the original permanent magnets. However, the main contributor to the cogging torque shifts from the 30th harmonic to the 42nd harmonic after the eccentric design. Moreover, the reason for the significant reduction in the cogging torque after the eccentric design can be explained in Figure 8b. It can be seen that the cogging torque generated by each harmonic order decreases to varying degrees. In addition, the cogging torque generated by the 6th and 30th harmonics exhibits an opposite trend to the total cogging torque. When the cogging torque generated by each harmonic order is superimposed, the cogging torque generated by the 6th and 30th harmonics is partially offset by that of the 18th and 42nd harmonics.

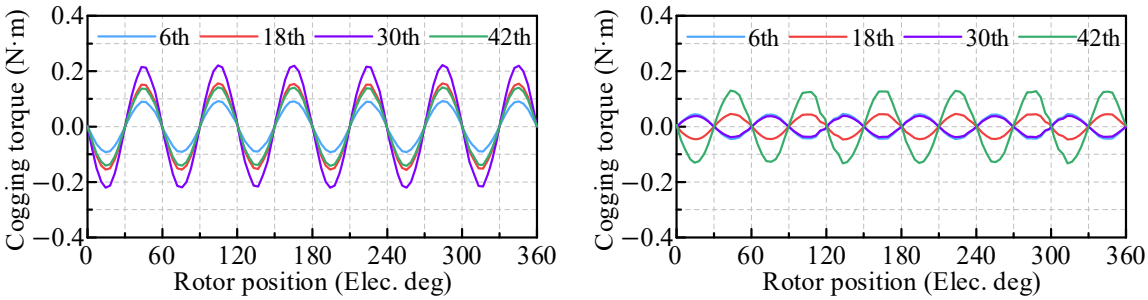

Figure 8. Cogging torque contribution of different harmonics. (**a**) PMSM with original permanent magnets. (**b**) PMSM with eccentric permanent magnets.

3.3. Effect of Harmonic Injection on Cogging Torque

The adoption of third harmonic injection to modify the permanent magnet can reduce the decrease in average torque while maintaining low cogging torque, thereby ensuring good torque performance. However, third harmonic injection significantly affects the air gap length and the air gap magnetic density. If the harmonic injection is not appropriate, it may lead to an increase in cogging torque and torque ripple. Therefore, it is essential to determine the suitable third harmonic injection amplitude to achieve torque output. The application of harmonic injection in the permanent magnet is shown in Figure 9. The maximum value of the outside radius OA_2 is determined by the amplitude of the third harmonic injected into the permanent magnet. Although the outside radius OA_2 varies with the position angle θ, its maximum value, along with the maximum thickness of the permanent magnet h_m, remains constant at 38.5 mm and 5 mm, respectively. With the injection of the third harmonic, the variation in the permanent magnet thickness $\Delta h_m(\theta)$ can be expressed as

$$\Delta h_m(\theta) = m_a[\sin\theta + a_0 \sin(3\theta)] \tag{11}$$

where a_0 is the amplitude of the injected third harmonic and m_a varies with the amplitude of the injected third harmonic to ensure that the maximum thickness of the permanent magnet remains constant. Consequently, $\Delta h_m(\theta)$ should equal the maximum thickness of the permanent magnet Δm. The relationship between m_a and a_0 can be expressed as

$$m_a = \frac{1}{8a_0}\left(\frac{3a_0+1}{12a_0}\right)^{-\frac{3}{2}}\Delta m \tag{12}$$

According to the geometric relationship in Figure 9, the outside radius OA_2 of the permanent magnet with third harmonic injection can be expressed as

$$OA_2 = R_m(\theta) = \Delta h_m(\theta) + OB = a\sin(\theta) + b\sin(3\theta) + OB \tag{13}$$

where a and b are constants. The maximum thickness of the permanent magnet Δm is 3 mm, and the values of a and b are calculated to be 3.41 and 0.414, respectively.

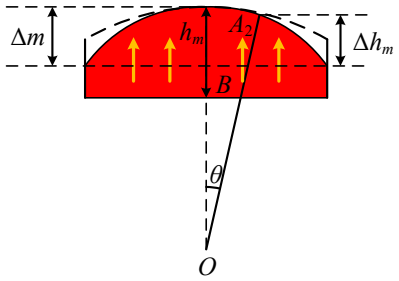

Figure 9. Permanent magnet with third harmonic injection.

The combination of the finite element and analytical method is used to evaluate the electromagnetic performance of the PMSM with third harmonic injection. The cogging torque is compared and analyzed, both with and without third harmonic injection, as shown in Figure 10a. It can be seen that the peak cogging torque of the PMSM with third harmonic injection is 0.23 N·m, with a reduction of 0.39 N·m. The contribution of each harmonic order to the cogging torque is shown in Figure 10b. The variation trend of the cogging torque resulting from the superposition of each harmonic is consistent with that obtained from the finite element simulation. The 30th harmonic is the dominant contributor to the cogging torque of the PMSM with third harmonic injection. Additionally, there is a significant reduction in the cogging torque generated by the 6th harmonic. The cogging torque generated by the 6th and 30th harmonics is nearly zero.

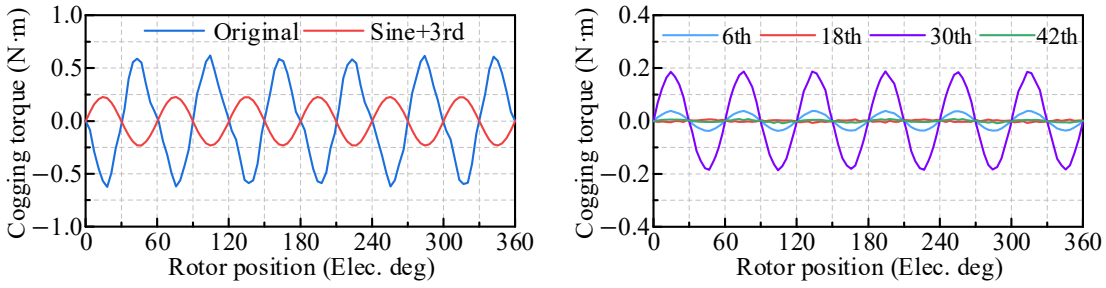

(**a**) (**b**)

Figure 10. Cogging torque of PMSM with harmonic injection. (**a**) Effect of harmonic injection. (**b**) Contribution of harmonics.

4. Electromagnetic Performance Analysis

Based on the analysis of the torque performance of the PMSM with different permanent magnet structures, the structure with permanent magnets having a 20 mm eccentricity is selected as the final design proposal. Therefore, the final finite element model of the PMSM is determined. The electromagnetic performance of the PMSM for FESS can be simulated and analyzed by using the Ansys Maxwell 2022R1 software. In finite element analysis, a boundary condition with zero magnetic flux is set outside the PMSM model. In addition, the simulation results are exported by finite element software and plotted in Origin 2019b software. The load magnetic field line distribution of the PMSM is shown in Figure 11a. It can be seen that the magnetic field line distribution is symmetrical, with each magnetic field line being nearly perpendicular to the air gap, thereby forming a closed magnetic circuit. In addition, the load magnetic flux density distribution of the PMSM is depicted in Figure 11b. It is apparent that no saturation occurs in the PMSM, and the magnetic flux density in the stator and rotor core yokes is relatively low. The magnetic flux density in the stator teeth, influenced by the number of pole-pairs, is significantly higher, with the maximum value reaching approximately 1.5 T.

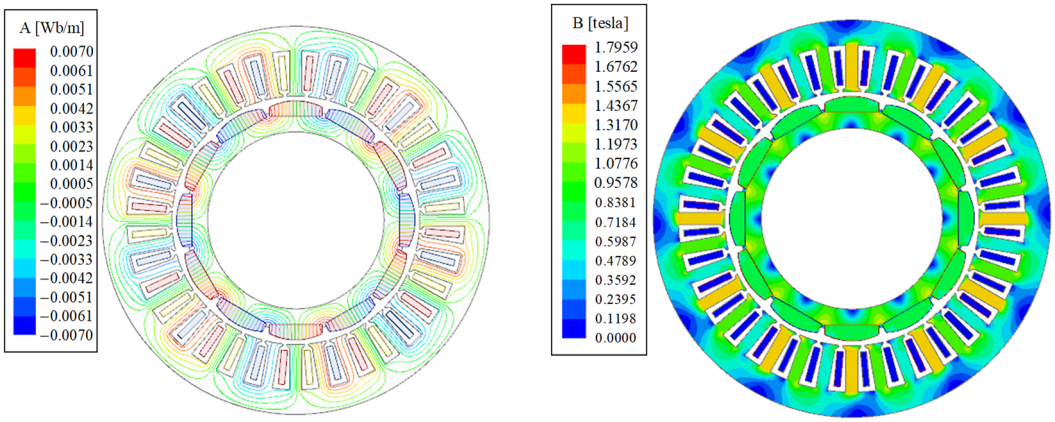

Figure 11. Load electromagnetic performance. (**a**) Magnetic field line. (**b**) Magnetic flux density.

The no-load back electromotive force of the PMSM is solved by finite element analysis, as shown in Figure 12. It is observed that the peak no-load back electromotive force is 257 V at a speed of 2500 rpm, and the no-load back electromotive force coefficient is 0.103 V/rpm. The no-load back electromotive force waveform exhibits excellent sinusoidal characteristics. Additionally, the torque performance of the PMSM with eccentric permanent magnets is shown in Figure 13. It is evident that the cogging torque of the PMSM is only 0.11 N·m. The torque fluctuates between 10.42 N·m and 10.75 N·m, with an average torque of 10.55 N·m. The torque waveform of the PMSM is smooth, with a torque ripple of only 3.1%, all due to the eccentric structure of the permanent magnets. Moreover, the vibration acceleration of the PMSM is analyzed and compared, both with and without eccentric permanent magnets, as shown in Figure 14. It can be seen that the vibration acceleration of the PMSM with eccentric permanent magnets is significantly lower than that of the PMSM with original permanent magnets.

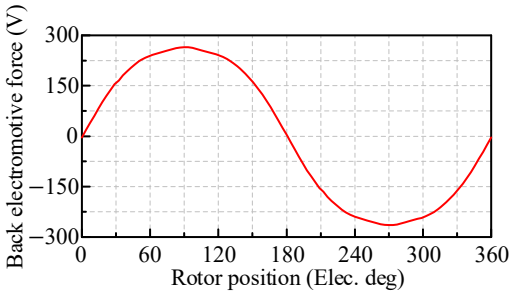

Figure 12. Back electromotive force of PMSM.

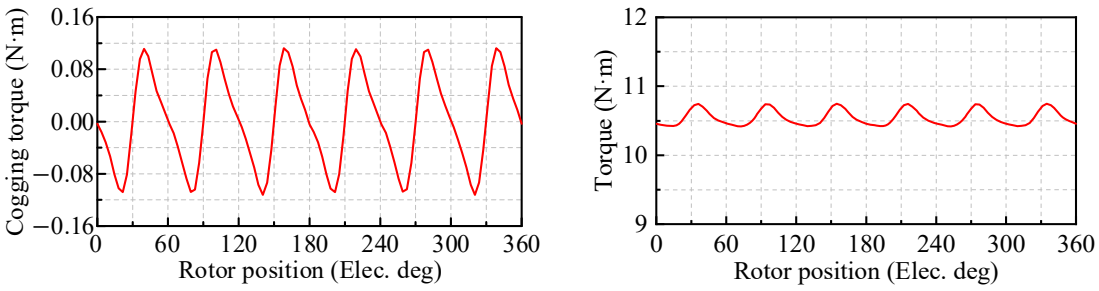

Figure 13. Torque performance of PMSM. (**a**) Cogging torque. (**b**) Torque.

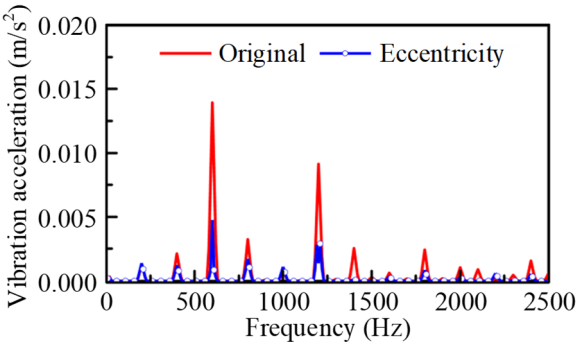

Figure 14. Vibration acceleration of PMSM with different permanent magnets.

5. Experimental Validation

Based on the theoretical analysis above, the proposed low torque ripple PMSM for FESS can be built and tested. When manufacturing the prototype, attention must be given to the magnetization direction of the permanent magnets, the dimensional accuracy of the machine components, and the potential for permanent magnets to detach during operation. The photograph of the prototype is shown in Figure 15. The permanent magnets are eccentric, with an eccentricity of 20 mm. To mitigate the risk of the permanent magnets detaching from the rotor core, a sheath made of carbon fiber is added to the rotor surface. The experimental platform of the prototype is set up, as shown in Figure 16. It can be seen that the experimental platform consists of two machines, a machine controller, and an oscilloscope. One of the two machines drives the other machine and connects an oscilloscope to the terminals of the three-phase winding. When one machine drives the other machine to run, the oscilloscope displays the no-load phase voltages of the PMSM. The actual speed of the PMSM can be estimated from the frequency displayed on the oscilloscope. The vibration and noise test platform of the prototype is shown in Figure 17. The platform primarily consists of a machine driver, a data acquisition system, a sound pressure probe and an oscilloscope. In this experiment, the acceleration measurement probe is fixed to the outer surface of the machine to measure the vibration and noise.

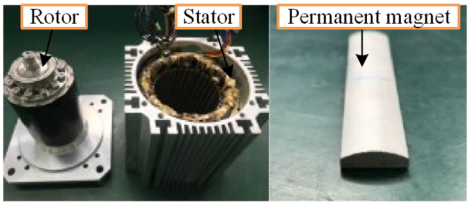

Figure 15. Prototype.

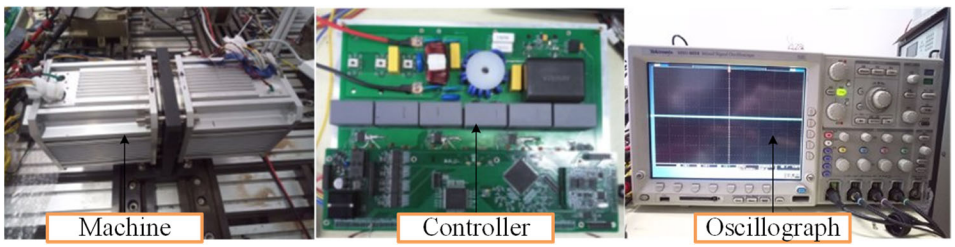

Figure 16. Experimental platform.

The no-load back electromotive force waveform of the PMSM for FESS is measured at a speed of 2500 rpm, as shown in Figure 18a. It can be seen that the waveform of the no-load back electromotive force is sinusoidal, with little harmonic content. The amplitude of each phase is approximately 240 V, indicating no asymmetry in amplitude. The experimental and simulated values of the no-load back electromotive force at various speeds are compared

and analyzed, as shown in Figure 18b. The experimental back electromotive force coefficient is calculated to be 0.096 V/rpm, which is slightly lower than the simulated value. The discrepancy between the simulated and experimental no-load back electromotive force coefficient of the PMSM remains constant. Consequently, as the rotational speed increases, the discrepancy between the simulated and experimental no-load back electromotive force also grows.

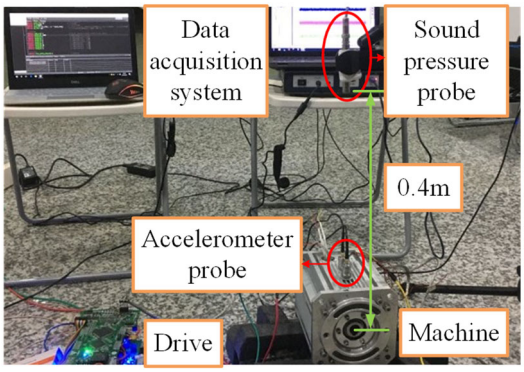

Figure 17. Vibration and noise test platform.

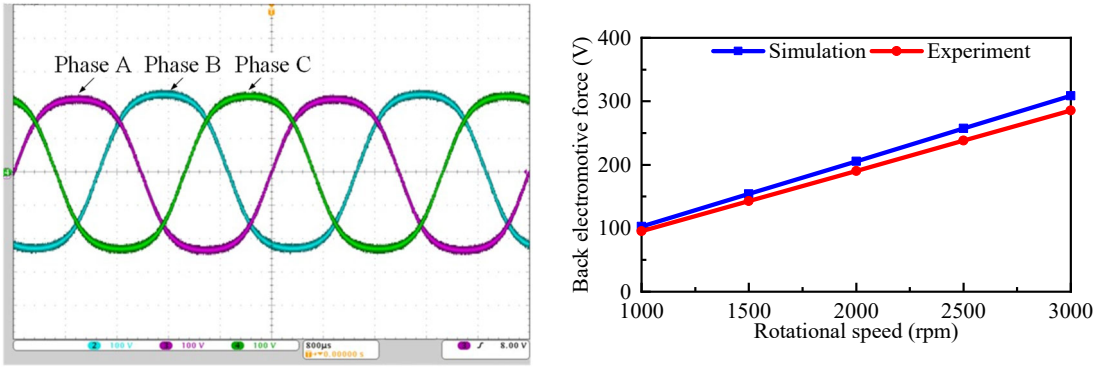

(**a**) (**b**)

Figure 18. Comparison of experimental and simulated results. (**a**) Back electromotive force of prototype. (**b**) Comparison of back electromotive force coefficient.

In addition, the torque of the PMSM for FESS is controlled by proportional integral derivative control and measured at a speed of 2500 rpm, as shown in Figure 19a. It can be observed that the average torque is 10.06 N·m, which is only 0.49 N·m lower than the simulated result. The torque ripple of the PMSM for FESS is only 3.9%, which is 0.8% higher than the simulated result. Consequently, a slight error exists between the experimental and simulated results. The error is mainly due to the processing and manufacturing inaccuracies, as well as the failure to account for the stacking coefficient and magnetic flux leakage at the ends during the simulation. Moreover, the vibration acceleration of the PMSM for FESS is measured and shown in Figure 19b. It is evident that the vibration acceleration at frequencies of 600 Hz and 1200 Hz is prominent. The vibration acceleration amplitude of the machine decreases significantly due to the eccentric design of the permanent magnet, which closely matches the simulation results.

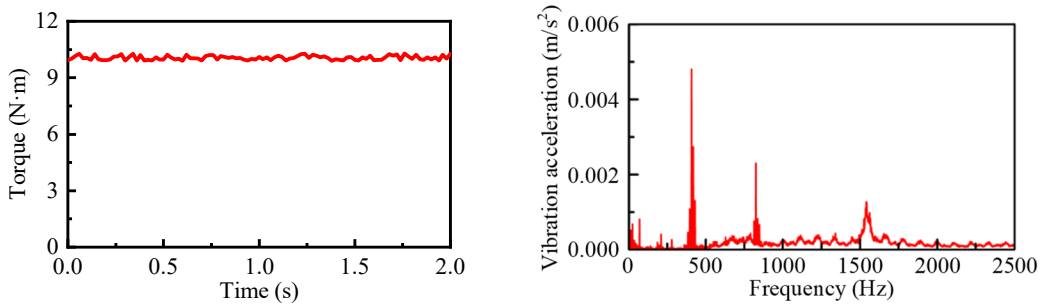

Figure 19. Experimental results. (**a**) Torque. (**b**) Vibration acceleration.

6. Discussion

This article analyzes the effects of eccentric permanent magnets and harmonic injection on cogging torque. By calculating the contribution of each harmonic order to the cogging torque, the underlying causes of torque ripple reduction are clarified. The contribution of each harmonic order to the cogging torque under different PMSMs is listed in Table 3. It can be seen that the eccentric permanent magnets and harmonic injection have varying degrees of impact in reducing the cogging torque generated by different harmonics. The cogging torque of the PMSM with eccentric permanent magnets is only 0.11 N·m, which is 0.12 N·m lower than that of the PMSM with harmonic injection. Additionally, the torque performance of the PMSM with different permanent magnets is listed in Table 4. It is evident that the average torque of the PMSM with harmonic injection is 10.67 N·m, only 0.12 N·m higher than that of the PMSM with eccentric permanent magnets. However, the torque ripple of the PMSM with eccentric permanent magnets is significantly lower than that of the PMSM with harmonic injection. Consequently, the prototype of the PMSM with permanent magnets exhibiting a 20 mm eccentricity is built to verify the theoretical analysis.

Table 3. Contribution of each harmonic order to cogging torque under different PMSMs.

Harmonic Order	Original PMSM	PMSM with Eccentric Permanent Magnets	PMSM with Harmonic Injection
6th	0.09 N·m	−0.04 N·m	0.04 N·m
18th	0.17 N·m	0.05 N·m	−0.01 N·m
30th	0.22 N·m	−0.04 N·m	0.19 N·m
42nd	0.14 N·m	0.14 N·m	0.01 N·m

Table 4. Torque performance of PMSM with different permanent magnets.

Machine	Average Torque	Torque Ripple
PMSM with eccentric permanent magnets	10.55 N·m	3.1%
PMSM with harmonic injection	10.67 N·m	7.9%

7. Conclusions

In this article, a PMSM with eccentric permanent magnets was proposed to reduce torque ripple in FESS. The cogging torque of the PMSM was investigated using a combination of finite element analysis and the analytical method. The effect of the permanent magnet with different shapes on cogging torque was analyzed, and the contribution of each harmonic order to the cogging torque was calculated. By altering the shape of the permanent magnets, the cogging torque induced by harmonic orders was reduced, thereby decreasing the overall cogging torque of the PMSM. Compared the cogging torque under different permanent magnets, the eccentric permanent magnets were finally adopted for the PMSM. Moreover, the electromagnetic performance of the PMSM was analyzed. Due

to the eccentric design of the permanent magnets, the torque ripple of the PMSM was only 3.1%. Additionally, a 36-slot 12-pole surface-mount PMSM was fabricated, and an experimental platform was built and tested. The no-load back electromotive force and torque were measured, and the error between the experimental and simulated results was no more than 7%. In addition, the experimental results showed that the torque ripple of the prototype was only 3.9%, which closely matched the simulation results. The vibration acceleration of the prototype was measured to verify the accuracy of the theoretical analysis. The experimental and simulated results were in good agreement.

Author Contributions: Conceptualization, Z.Z.; methodology, Q.Z.; software, Y.S.; validation, Z.Z.; investigation, Y.S.; resources, Y.S.; data curation, Y.S.; writing—original draft preparation, Y.S.; writing—review and editing, Z.Z.; visualization, Y.S.; supervision, Z.Z.; project administration, Y.S.; funding acquisition, Q.Z. All authors have read and agreed to the published version of the manuscript.

Funding: This work was fully funded by the Zhenjiang Key R&D Plan (Industry Foresight and Common Key Technology), Project Award Number: GY2023001.

Data Availability Statement: Data are contained within the article.

Conflicts of Interest: The authors declare no conflicts of interest.

References

1. Dai, X.; Ma, X.; Hu, D.; Duan, J.; Chen, H. An overview of the R&D of flywheel energy storage technologies in China. *Energies* **2024**, *17*, 5531. [CrossRef]
2. Samineni, S.; Johnson, B.K.; Hess, H.L.; Law, J.D. Modeling and analysis of a flywheel energy storage system for voltage sag correction. *IEEE Trans. Ind. Appl.* **2006**, *42*, 42–52. [CrossRef]
3. Huang, D.; Jiao, C.; Fang, J. Design and research of a high-temperature superconducting flywheel energy storage system with zero-flux coils. *IEEE Trans. Appl. Supercon.* **2024**, *34*, 5702406. [CrossRef]
4. Li, X.; Anvari, B.; Palazzolo, A.; Wang, Z.; Toliyat, H. A utility-scale flywheel energy storage system with a shaftless, hubless, high-strength steel rotor. *IEEE Trans. Ind. Electron.* **2018**, *65*, 6667–6675. [CrossRef]
5. Abdeltawab, H.H.; Mohamed, Y.A.-R.I. Robust energy management of a hybrid wind and flywheel energy storage system considering flywheel power losses minimization and grid-code constraints. *IEEE Trans. Ind. Electron.* **2016**, *63*, 4242–4254. [CrossRef]
6. Du, Z.S.; Lipo, T.A. High torque density and low torque ripple shaped-magnet machines using sinusoidal plus third harmonic shaped magnets. *IEEE Trans. Ind. Appl.* **2019**, *55*, 2601–2610. [CrossRef]
7. Kwon, J.-W.; Kwon, B.-I. High-efficiency dual output stator-PM machine for the two-mode operation of washing machines. *IEEE Trans. Energy Convers.* **2018**, *33*, 2050–2059. [CrossRef]
8. Bramerdorfer, G. Multiobjective electric machine optimization for highest reliability demands. *CES Trans. Electr. Mach. Syst.* **2020**, *4*, 71–78. [CrossRef]
9. Zhang, W.; Li, Y.; Wu, G.; Rao, Z.; Gao, J.; Luo, D. Robust predictive power control of *N**3-phase PMSM for flywheel energy storage systems application. *Energies* **2021**, *14*, 3684. [CrossRef]
10. Ye, C.; Yu, D.; Liu, K.; Dai, Y.; Deng, C.; Yang, J.; Zhang, J. Research of a stator PM excitation solid rotor machine for flywheel energy storage system. *IEEE Trans. Ind. Electron.* **2022**, *69*, 12140–12151. [CrossRef]
11. Urresty, J.-C.; Riba, J.-R.; Romeral, L.; Garcia, A. A simple 2-D finite-element geometry for analyzing surface-mounted synchronous machines with skewed rotor magnets. *IEEE Trans. Magn.* **2010**, *46*, 3948–3954. [CrossRef]
12. Ye, S.; Zhou, D.; Yao, X.; Blaabjerg, F. Component-level reliability assessment of a direct-drive PMSG wind power converter considering two terms of thermal cycles and the parameter sensitivity analysis. *IEEE Trans. Power Electron.* **2021**, *36*, 10037–10050. [CrossRef]
13. Tong, W.; Sun, L.; Wu, S.; Hou, M.; Tang, R. Analytical model and experimental verification of permanent magnet eddy current loss in permanent magnet machines with nonconcentric magnetic poles. *IEEE Trans. Ind. Electron.* **2022**, *69*, 8815–8824. [CrossRef]
14. Yamada, Y.; Sugimoto, H.; Imae, K. Efficiency improvement of permanent magnet synchronous machines with high slot fill aluminum winding. In Proceedings of the 2022 IEEE Energy Conversion Congress and Exposition, Detroit, MI, USA, 9–13 October 2022; pp. 1–6.
15. Aydin, M.; Gulec, M. Reduction of cogging torque in double-rotor axial-flux permanent-magnet disk motors: A review of cost-effective magnet-skewing techniques with experimental verification. *IEEE Trans. Ind. Electron.* **2014**, *61*, 5025–5034. [CrossRef]
16. Zhu, X.; Hua, W.; Wu, Z.; Huang, W.; Zhang, H.; Cheng, M. Analytical approach for cogging torque reduction in flux-switching permanent magnet machines based on magnetomotive force-permeance model. *IEEE Trans. Ind. Electron.* **2018**, *65*, 1965–1979. [CrossRef]

17. Wang, T.; Zhu, X.; Xiang, Z.; Fan, D.; Quan, L. Torque ripple suppression of a permanent magnet vernier motor from perspective of shifted air-gap permeance distribution. *IEEE Trans. Magn.* **2022**, *58*, 8203006. [CrossRef]
18. Du, Z.S.; Lipo, T.A. Reducing torque ripple using axial pole shaping in interior permanent magnet machines. *IEEE Trans. Ind. Appl.* **2020**, *56*, 148–157. [CrossRef]
19. Wu, L.; Lyu, Z. Harmonic injection-based torque ripple reduction of PMSM with improved DC-link voltage utilization. *IEEE Trans. Power Electron.* **2023**, *38*, 7976–7981. [CrossRef]
20. Shimizu, Y.; Morimoto, S.; Sanada, M.; Inoue, Y. Investigation of rotor topologies for reducing torque ripple in double-layer IPMSMs for automotive applications. *IEEE Trans. Ind. Electron.* **2023**, *70*, 8276–8285. [CrossRef]
21. Xu, M.; Zhao, W.; Ji, J.; Chen, Q.; Liu, G. Auxiliary notching rotor design to minimize torque ripple for interior permanent magnet machines. *IEEE Trans. Ind. Electron.* **2024**, *71*, 12051–12062. [CrossRef]
22. Zhu, Z.Q.; Wu, L.J.; Xia, Z.P. An accurate subdomain model for magnetic field computation in slotted surface-mounted permanent-magnet machines. *IEEE Trans. Magn.* **2010**, *46*, 1100–1115. [CrossRef]
23. Chen, Z.; Xia, C.; Geng, Q.; Yan, Y. Modeling and analyzing of surface-mounted permanent-magnet synchronous machines with optimized magnetic pole shape. *IEEE Trans. Magn.* **2014**, *50*, 8102804. [CrossRef]